

Defects of perovskite semiconductor CsPbBr₃ investigated via photoluminescence and thermally stimulated current spectroscopies

Cite as: J. Appl. Phys. 134, 245101 (2023); doi: 10.1063/5.0177809

Submitted: 24 September 2023 · Accepted: 7 December 2023 ·

Published Online: 26 December 2023



Zhifu Liu,¹ John A. Peters,^{1,2} Khasim Saheb Bayikadi,³ Vladislav Klepov,³ Lei Pan,³ Indra Raj Pandey,³ Mercouri G. Kanatzidis,^{3,a)} and Bruce W. Wessels^{1,a)}

AFFILIATIONS

¹Department of Materials Science and Engineering, Northwestern University, Evanston, Illinois 60208, USA

²Department of Chemistry, Physics & Engineering Studies, Chicago State University, Chicago, Illinois 60608, USA

³Department of Chemistry, Northwestern University, Evanston, Illinois 60208, USA

Note: This paper is part of the Special Topic on Native Defects, Impurities and the Electronic Structure of Compound Semiconductors: A Tribute to Dr. Wladyslaw Walukiewicz.

^{a)}Authors to whom correspondence should be addressed: m-kanatzidis@northwestern.edu and b-wessels@northwestern.edu

ABSTRACT

Halide perovskites are essential materials for hard radiation detectors at ambient temperature. To improve detector performance, charge transport must be investigated and optimized. Using photoluminescence (PL) and thermally stimulated current (TSC) spectroscopies, we investigate photogenerated charge carriers in Bridgman-grown CsPbBr₃ single crystals to understand the nature of charge transport. PL spectroscopy of these halide perovskites revealed the presence of strong emission bands at the band edge, which were attributed to free or bound excitons. It is shown that a wide broadening of the excitonic linewidth in these halide perovskites arises from strong exciton–phonon coupling, which is substantially dominated by longitudinal optical phonons via Fröhlich interaction. An additional contribution due to the presence of ionized impurities was also observed. Crystals with a detectable sensitivity to high-energy gamma radiation are characterized by a higher intensity and a narrower linewidth of the principal PL peak at 2.326 eV. Defect states beyond 2.214 eV have a negative impact on detector sensitivity to high-energy gamma radiation. TSC spectroscopy reveals an array of trap levels spanning 0.15–0.70 eV, attributed to intrinsic point defects and multiple extrinsic defects involving dopants or impurities. Defects identified included Cs and Br vacancies, as well as Pb interstitials with concentrations in the 10¹¹–10¹⁶ cm^{−3} range. Understanding how the synthesis process impacts the types and concentrations of the defects present is currently under investigation. Elimination or suppression of the defect/trap states should result in halide perovskite materials with longer carrier diffusion lengths and improved detector characteristics.

Published under an exclusive license by AIP Publishing. <https://doi.org/10.1063/5.0177809>

INTRODUCTION

There are various potential uses for halide perovskites, including light-emitting diodes (LEDs) and hard radiation detectors that operate at room temperature. Due to their favorable physical features and relatively high atomic number elements, halide perovskites have found applications in ionizing radiation detector systems. In addition, their high bulk resistivity ensures low noise and low dark currents in these detector systems. Using CsPbBr₃ perovskite, we have recently demonstrated high resolution radiation detectors with excellent energy resolution.^{1–3} The study examined

and characterized the inherent structural defects and carrier trap states in CsPbBr₃ halide perovskites using photoluminescence (PL) and thermally stimulated current (TSC) spectroscopy methods. Both PL and TSC are essential techniques for probing and understanding semiconductor materials. In addition to providing information regarding crystalline quality, they identify and quantify defects and impurities in semiconductors. Although perovskites are commonly regarded as being “defect tolerant,”⁴ their defects are not solely attributed to impurities. Structural disorders such as vacancies, deviations from stoichiometry, domain formation,

30 December 2023 08:30:28

TABLE I. Crystal identification, characterization, detector performance information.

Crystal ingot ID	Characterization technique	Detector performance reported
KS15C	1. Laser power dependent PL 2. Surface PL for spatial disorder	Ref. 8
VK59A	1. Temperature dependent PL 2. Laser power dependent PL 3. Gamma irradiation	Ref. 9
VK74A	1. TSC	Supplementary material and Ref. 10
IP21009	1. TSC 2. X-ray irradiation	Unpublished results

twinning, and lattice distortion (potentially coupled with local strain), also contribute to these defects. Defects are not only capable of acting as nonradiative recombination centers, but they can also induce photoluminescence. When considering carrier dynamics and radiative efficiency, the impact of structural disorder is most evidently seen in two key ways. First, there is a reduction in carrier recombination lifetime and mobility, which directly leads to a suppression of emission. Second, the disorder causes broadening of the photoluminescence (PL) spectrum. To fully understand these phenomena and their influence on detector efficiency, it is crucial not only to study in detail the underlying charge dynamics within the crystals but also to work toward optimizing these processes for better performance.^{5,6} The utilization of thermally stimulated current (TSC) spectroscopy proved to be a viable approach in the assessment of defect levels and concentrations within CsPbBr₃ crystals.⁷ Gaining a more comprehensive understanding of the defect physics in metal halide perovskites provides crucial insights for the future development of effective radiation detectors based on halide perovskites.

In this work, we investigated the physical and charge transport properties of melt-grown single crystals of CsPbBr₃ using PL and TSC spectroscopy. The detector performance of these crystals was determined to be highly dependent on their defect concentration and electronic structure. New insights into the correlations between semiconductor defects, dopant impurities, and optical and transport properties are also discussed. Excitons in Bridgman-grown CsPbBr₃ single crystals were examined using photoluminescence (PL) spectroscopy to determine the nature of the electronic states. The PL is sensitive to defects at a variety of locations throughout a sample's surface. A high PL intensity for the primary exciton peak and a minimal contribution from band edge states are indicative of good quality and homogeneous crystals. A comparative and in-depth examination of multiple CsPbBr₃ crystals revealed that the TSC approach is sensitive to defect densities in the range of 10^{11} – $10^{17}/\text{cm}^3$ and can differentiate $\sim 10\%$ and $\sim 0.5\%$ variations in trap concentrations in 10^{11} and $10^{17}/\text{cm}^3$ regimes, respectively. The findings obtained from a comparative analysis of TSC spectroscopy measurements conducted on a reference sample and a sample that had been subjected to an external electric field indicate that the biased sample exhibits significantly reduced defect densities. Furthermore, this biased sample exhibits an improved spectral response upon exposure to a radiation source, details of which are reported elsewhere.⁸

RESULTS AND DISCUSSION

Characterization and analysis were performed on five CsPbBr₃ single crystals that were produced using the Bridgman method. Table I presents the crystal identification and characteristics of the samples utilized in the present study. The findings corroborate our research on the spectral sensitivity of defect-tolerant CsPbBr₃ detectors when subjected to high-energy radiation sources.^{8–10} We effectively correlate the PL and TSC measurement data with detector crystal sensitivity to high-energy gamma radiation.

Photoluminescence (PL) study on defect states that may affect performance of radiation detectors

Photoluminescence spectroscopy measurements were carried out on samples KS15C-xy2, VK59A_ref, and VK59A_bb. Details of the PL setup can be found in the SI document, as well as our previous article.¹¹

As shown in Fig. 1, with sample KS15C-xy2 cut in parallel to the growth direction (the x-y cut orientation), individual room temperature photoluminescence profiles vs laser power can be deconvoluted into multiple peaks. The excitation power dependence of the PL intensity (Fig. 1) reflects the type of recombination

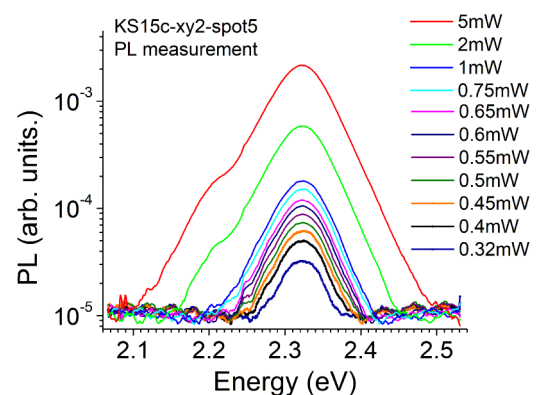


FIG. 1. Typical PL signal vs photon energy with varying laser powers on spot 5 of sample KS15c-xy2. Datasets are taken at room temperature. The sample surface area is $\sim 21.3 \text{ mm}^2$ and the laser spot size is $\sim 0.61 \text{ mm}^2$.

30 December 2023 08:30:28

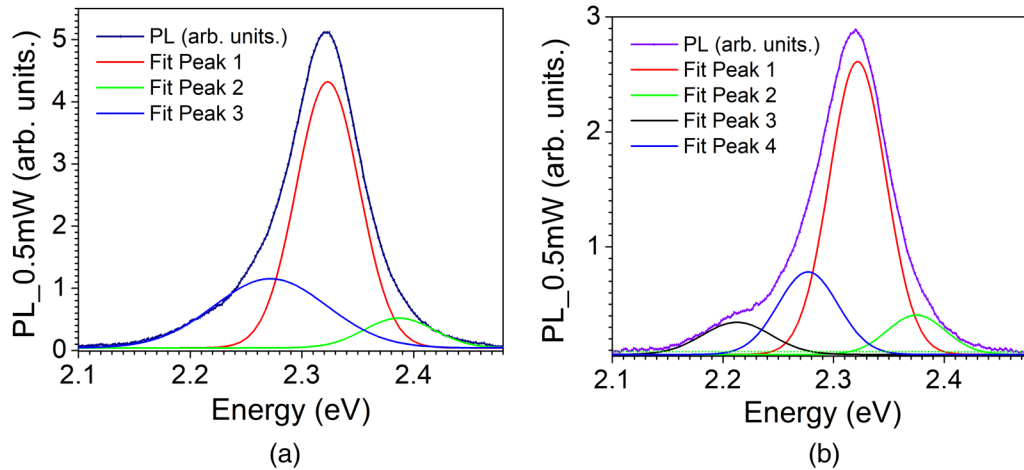


FIG. 2. PL spectra of spot 1 (left) and spot 2 (right) on sample KS15c-xy2, under laser power of 0.5 mW. The sample surface area is $\sim 21.3 \text{ mm}^2$ and the laser spot size is $\sim 0.61 \text{ mm}^2$.

processes in Bridgman-grown crystals. The intensity I of the luminescence emission is proportional to L^γ , where L is the power of the exciting laser radiation. An exponent (γ) value in the range of $1 < \gamma < 2$ indicates exciton-like transitions.¹² The primary peak is centered at approximately 2.326 eV (533 nm). The value of γ suggests the presence of excitonic behavior in the observed peaks. The observed spectral peaks at approximately 2.2752 eV (545 nm) and 2.2222 eV (558 nm) are provisionally attributed to bound excitons that are associated with intrinsic point defects.

Assuming that all crystals exhibit a certain degree of disorder, it is essential to determine the degree of their spatial inhomogeneity, which is determined by the static component of the disorder (i.e., vacancies, deviation from stoichiometry). In this regard, PL measured at various locations on the sample can distinguish between disorders acting on a macroscale (i.e., over lengths greater than one micrometer) and a sub-micrometer scale. PL measurements taken from various locations within the CsPbBr₃ sample are compared and contrasted in Fig. 2. As can be observed in Fig. 2, PL spectroscopy is highly sensitive to surface quality and defects of spots in close proximity. The intensity of the principal PL peak at 2.326 eV (533 nm) is significantly higher at spot 1 than at spot 2. Furthermore, it can be seen that spot 1 behaves differently compared to spot 2, with the latter showing a significant contribution from band edge states beyond about 2.214 eV (560 nm). In the presence of a relevant contribution of static disorder, we expect to detect changes in the low energy band tail, depending on the excited spot in the sample. Significant variations in the low energy exponential branch of the PL spectra correspond to the presence of static disorder in the Urbach band tail, such as vacancies and stoichiometry deviations. CsPbBr₃ crystals with a detectable sensitivity to high-energy gamma radiation are characterized by a higher intensity and a narrower linewidth of the principal PL peak at 2.326 eV (533 nm). The presence of extended defect states (beyond 2.214 eV) reduces the sensitivity of a crystal detector to gamma

radiation. It is anticipated that crystals of superior quality and uniformity will exhibit significant photoluminescence (PL) intensity for the primary peak at around 2.326 eV (533 nm), while displaying minimal influence from band edge states, beyond approximately 2.214 eV (560 nm).

We conducted a temperature-dependent PL study on the CsPbBr₃ sample. Figure 3 presents the PL spectra as a function of temperature for a melt-grown CsPbBr₃ sample (VK59A_ref). The PL intensity is plotted on a semi-logarithmic scale, with photon energy as the independent variable, for each spectrum. Continuous wave (CW) excitation at an energy of 3.062 eV (corresponding to a wavelength of 405 nm), significantly above the bandgap energy of the CsPbBr₃ compound, was employed.

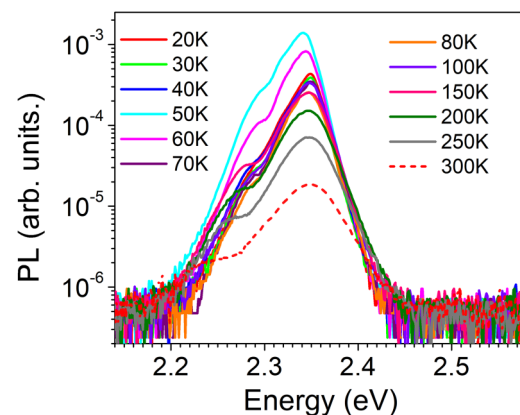


FIG. 3. PL spectra vs photon energy as a function of temperature T at excitation power of 2 mW for sample VK59A_ref.

30 December 2023 08:30:28

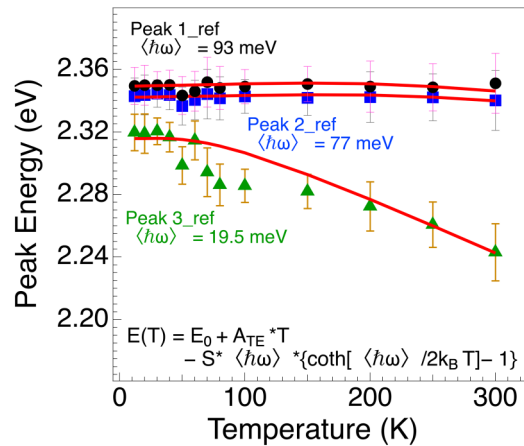


FIG. 4. Peak energy of deconvoluted PL peaks vs temperature for sample VK59A_ref.

As anticipated, the PL spectra, primarily comprised of exciton emission, reveal a prominent central peak accompanied by exponential decay tails. At temperatures below 100 K, the photoluminescence (PL) peak has a core Gaussian distribution with a discernible shoulder on the lower energy side. The prominence of this shoulder varies across different samples. The observed emission from this shoulder can be attributed to the localized or bound excitons. The existence of disorder is indicated by the Gaussian shape of the photoluminescence (PL) peak. Thermal expansion broadens the PL. The PL spectra also show two other noteworthy characteristics: a high-energy tail and a low-energy tail, both of which have a roughly exponential form. The presence of a tail on the high-energy side, characterized by a temperature-dependent slope, is frequently observed in the photoluminescence spectra. The characteristics of the low energy excitonic tail are influenced by various factors such

as temperature, degree of disorder (i.e., point defects, deviation from stoichiometry), and impurity concentration. The existence of defects can cause the emergence of additional electronic local levels in the forbidden band, which leads to an energy loss due to lattice thermal vibration, or a radiative transition of trapped excitons, i.e., defect-induced luminescence.¹³ Vacancies are usually the most abundant native defects in halide perovskites.

The phenomenon of thermal quenching of near-band-edge PL in hybrid halide perovskites has been attributed by Baranowski¹⁴ to the process of thermalization of excitons, wherein trapped or bound excitons are transferred to the conduction band. The enhanced mobility and diffusion length of excitons/polarons in this context facilitate their diffusion and subsequent capture by non-radiative trapping centers located in close proximity to, or at, the surface. With the rise in temperature, the bound excitons undergo thermalization, transitioning into the conduction band, which is associated with greater mobilities. The involvement of phonons in the recombination process can be observed in previous studies on the dependence of the peak energy of PL on temperature, denoted as $E(T)$. These studies have shown that the luminescent peak shift is influenced by a combination of the interaction between electrons and phonons (EP interaction) and thermal expansion (TE), as described by the following equation:¹⁵

$$E(T) = E_0 + A_{TE}T - S\langle\hbar\omega\rangle[\coth(\langle\hbar\omega\rangle/2k_B T) - 1], \quad (1)$$

where E_0 is the peak energy at $T = 0$ K, A_{TE} is the thermal expansion parameter, S is the Huang–Rhys factor indicating electron–phonon coupling strength, and $\langle\hbar\omega\rangle$ is an average optical phonon energy. Based on an analysis of the peak energy data presented in Fig. 4, and employing Eq. (1), the average phonon energy $\langle\hbar\omega\rangle$ was determined to be 93, 77, and 19.5 meV for the main peak, shoulder peak, and low energy peak, respectively. The Huang–Rhys parameter for peak 3 is much larger than that of peak 2, indicating a relatively high level of coupling strength. The effective phonon energy values of 93, 77, and

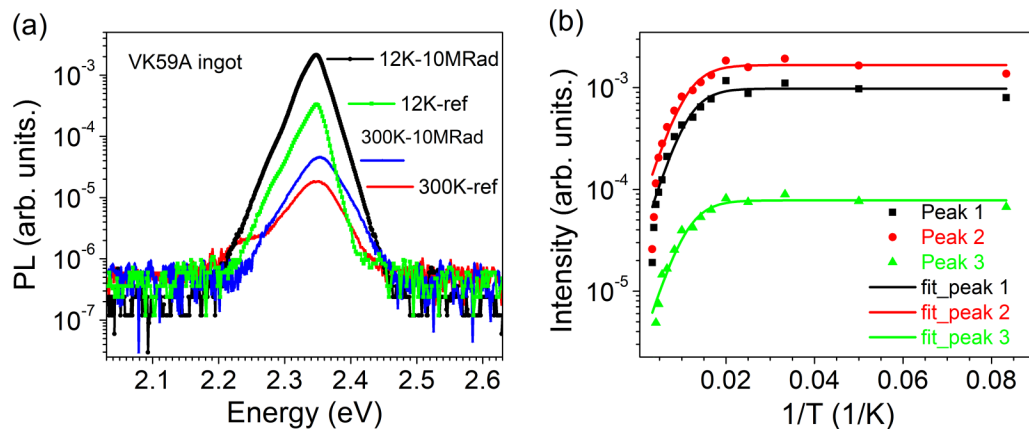


FIG. 5. (a) Temperature-dependent PL datasets of irradiated sample VK59A_bb (10 MRad) and of sample VK59A_ref. Only two temperatures (12, 300 K) are shown. (b) PL intensity of peaks in VK59A_bb vs $1/T$.

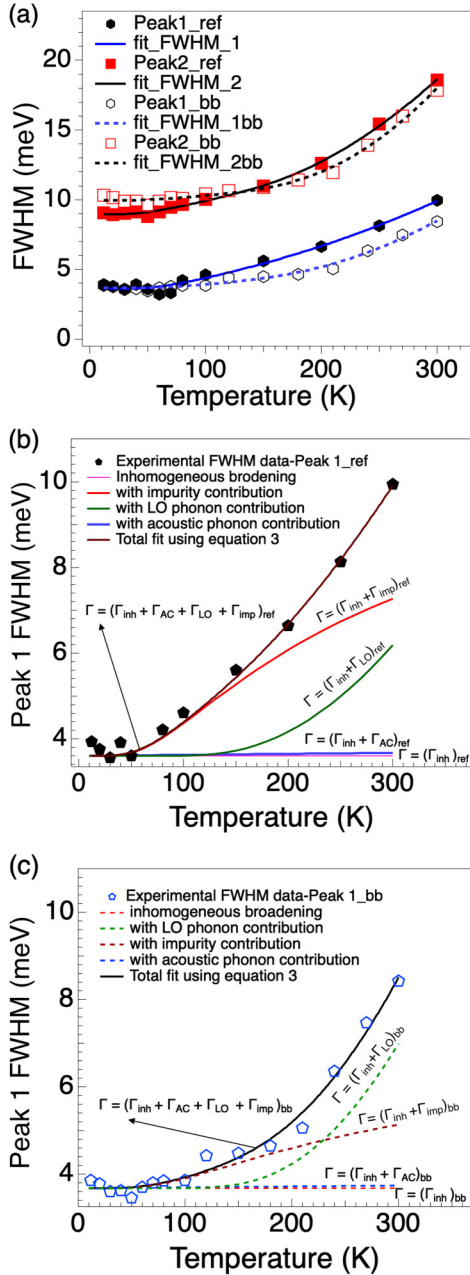


FIG. 6. (a) FWHM of peak vs temperature of VK59A_ref (solid dots), as compared to those of VK59A_bb (hollow dots). (b) The sum of inhomogeneous broadening and individual temperature-dependent linewidth broadening terms for Peak1_ref, and (c) the sum of inhomogeneous broadening and individual temperature-dependent linewidth broadening terms for Peak1_bb. The inhomogeneous broadening term itself, $\Gamma(T) = \Gamma_{inh}$ [horizontal solid (ref) and dashed (bb) red lines]; with the acoustic phonon interaction term, $\Gamma(T) = \Gamma_{inh} + \Gamma_{AC}$ (solid and dashed blue lines); with the LO phonon interaction term, $\Gamma(T) = \Gamma_{inh} + \Gamma_{LO}$ (solid and dashed green lines); with the impurity term, $\Gamma(T) = \Gamma_{inh} + \Gamma_{imp}$ (solid and dashed red lines). For each sample, the sum of all contributing terms, $\Gamma(T) = \Gamma_{inh} + \Gamma_{AC} + \Gamma_{LO} + \Gamma_{imp}$, is shown as well.

19.5 meV are consistent with previous Raman spectroscopy results.^{3,16} Theoretical Raman spectra of CsPbBr₃ from first-principles molecular dynamics (MD) simulations, based on density functional theory (DFT), reveal Raman vibrations at 76.4, 73.5, and 72.8 cm⁻¹ for the orthorhombic, tetragonal, and cubic phases, respectively.¹⁷ In addition, experimental Raman spectra of a CsPbBr₃ single crystal were found to be composed of three active Raman vibrations concentrated at 76, 135, and 311 cm⁻¹.¹⁸ Hence, we attribute the average phonon energy ($\hbar\omega$) of peak 3 (19 meV) to double the Raman mode at 76 cm⁻¹ while that of peak 2 (77 meV) corresponds to double the Raman mode at 311 cm⁻¹. The value of $\langle\hbar\omega\rangle$ for peak 1 (93 meV) can thus be assumed to correspond to double the sum of the Raman modes at 73 and 311 cm⁻¹. The peak at 76 cm⁻¹ has been attributed to the phonon vibration mode related to the motion of Cs⁺ and the vibration of [PbBr₆]⁴⁻, while the peak at 311 cm⁻¹ was related to the Raman second-order phonon scattering mode of CsPbBr₃.¹⁹

Study on ⁶⁰Co irradiation effect on perovskite CsPbBr₃ samples through PL spectroscopy

PL spectroscopy was employed to analyze CsPbBr₃ crystals that had been exposed to radiation as well as controlled reference crystals, and the results were compared. The samples were irradiated with gamma rays in a lead-lined chamber at Penn State University's Radiation Science and Engineering Center (RSEC) using ⁶⁰Co radiation sources. Samples were exposed to an isotropic dosage at a rate of 155 kRad h⁻¹ (air) in an ambient environment. Temperature-dependent PL spectra of reference and irradiated (10 MRad ⁶⁰Co exposure) crystals from a recent ingot (VK59A) can be deconvoluted into three distinct peaks with differing energy dependence. Low energy band tailing is evident in the reference sample, but it is not discernible in the irradiated sample [Fig. 5(a)]. The observed pattern suggests that there is no increase in the number of defect states when the sample is irradiated. Additionally, a reduction in peak broadening is observed in the sample that has been subjected to irradiation. For low excitation levels up to 2 mW, defect states are seen between 550 and 570 nm (2.2545–2.1754 eV). It is evident that the band tail-related peak or shoulder has a wide variety of features. These states may have an effect on the sample's behavior as a radiation detector.

Several physical parameters of CsPbBr₃ can be derived from the temperature-dependent PL analysis. These include the exciton binding energy (E_B), longitudinal optical (LO) phonon energy (E_{ph}), inhomogeneous broadening (Γ_o), exciton-acoustic phonon coupling coefficient φ_A , and the exciton-LO phonon coupling strength (φ_{LO}). As expected, the PL intensity for all observed peaks exhibits a decrease as the temperature increases. The PL intensity as a function of temperature is displayed and fitted with an Arrhenius equation,

$$I(T) = \frac{I_0}{(1 + Ce^{-E_B/k_B T})}, \quad (2)$$

where I_0 is the intensity at 0 K and k_B is the Boltzmann constant. Figure 5(b) shows the fitted curve using Eq. (2) for the irradiated sample VK59A_bb. The three calculated values of E_B for VK59A_bb are ~27 meV.

TABLE II. Comparison of fit values of FWHM for samples VK59A_bb and VK59A_ref.

	Γ_0 (meV)	φ_{LO} (meV)	E_{ph} (meV)	φ_{imp} (meV)	E_i (meV)
Peak 1, reference	3.60 ± 0.46	47.7 ± 13.4	76.81 ± 15.31	8.05 ± 0.31	20.34 ± 10.04
Peak 1, irradiated	3.67 ± 0.22	109.8 ± 23.4	91.24 ± 5.31	3.68 ± 0.09	23.92 ± 9.14
Peak 2, reference	8.95 ± 0.23	116.60 ± 19.80	76.0 ± 10.9	5.75 ± 0.24	15.74 ± 3.82
Peak 2, irradiated	9.96 ± 0.34	233.7 ± 35.2	92.5 ± 10.6	2.68 ± 0.06	18.20 ± 11.80

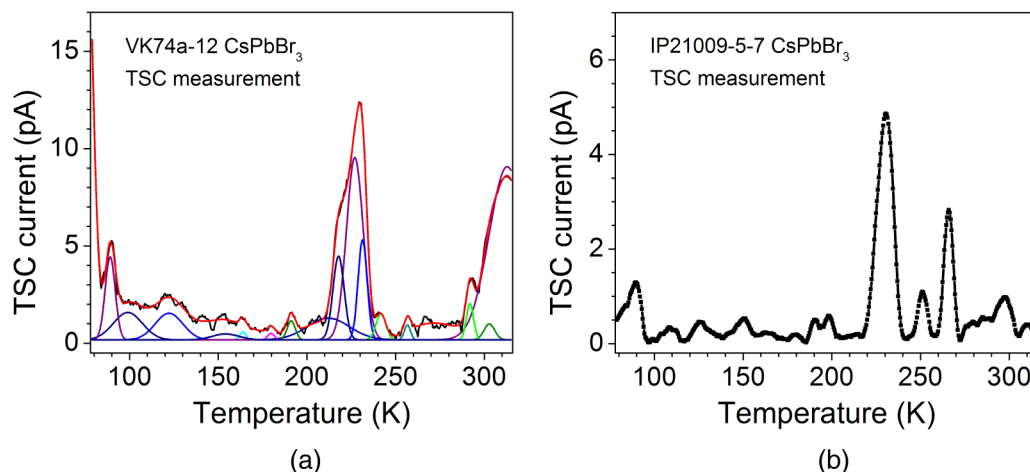
The linewidth of PL emission is an essential characteristic in optoelectronic and detector devices and is influenced by two distinct factors. The first is the temperature-independent inhomogeneous broadening, which arises from variations in size, shape, elemental composition, and other properties. The second factor is the temperature-dependent homogeneous broadening, which occurs due to the interaction between excitons and acoustic phonons, optical phonons, and impurities. The width of the PL emission line resulting from the combination of the two factors is described by the model²⁰

$$\begin{aligned}\Gamma(T) &= \Gamma_{inh} + \Gamma_{AC} + \Gamma_{LO} + \Gamma_{imp} \\ &= \Gamma_0 + \varphi_A T + \varphi_{LO} (e^{E_{ph}/k_B T} - 1) + \varphi_{imp} e^{-E_i/k_B T}.\end{aligned}\quad (3)$$

In Eq. (3), the first term, Γ_0 , is a temperature-independent term, which accounts for inhomogeneous line broadening induced by the inhomogeneity in size, shape, and composition of the crystal. The remaining three terms represent the homogeneous broadening. The second term is the exciton-acoustic phonon coupling's linear contribution to the linewidth. The third term characterizes the interaction between excitons and longitudinal optical (LO) phonons, whereas the last term indicates the impact of ionized defects or impurities on the linewidth. Defects/impurities may be present in the form of point defects or dislocations such as

twinning resulting from the cubic-to-tetragonal phase transition in CsPbBr₃. Figure 6(a) displays the FWHM of the PL emission peaks observed in both the reference sample (VK59A_ref) and the irradiated sample (VK59A_bb). The experimental data were fitted to Eq. (3) using the least squares method to achieve the best fits. The corresponding optimal fits are also depicted in Fig. 6(a). The incorporation of the impurity scattering component in Eq. (3) facilitates a highly reliable fit. The fitted values of the parameters Γ_0 , φ_{LO} , E_{ph} , φ_{imp} , and E_i , obtained from the fitting procedure, are displayed in Table II.

Figure 6(b) illustrates the distinct contributions of defect/impurity states, exciton-longitudinal optical phonon interactions, and exciton-acoustic phonon interactions to the broadening of peak 1. It is clearly evident that the influence of defect/impurity states on the PL broadening in the reference sample is significantly more pronounced than the contribution of LO phonons. Following irradiation, LO phonon contributions outweigh those from the defect/impurity states at higher temperatures (>230 K). Peak 2 exhibits a similar pattern. Based on the findings presented in Figs. 6(b) and 6(c), it can be inferred that the broadening of PL emission in CsPbBr₃ is a consequence of exciton-phonon coupling that is influenced by the material's polar nature. The primary factor contributing to this broadening is the interaction between carriers and longitudinal optical (LO) phonons, which can be classified as Fröhlich type carrier interaction. The presence of impurities results

**FIG. 7.** Comparison of TSC signal vs temperature of two samples. (Left) reference CsPbBr₃ sample VK74a-12, (right) CsPbBr₃ sample IP21009-5-7, exposed to an x-ray beam with an energy of 58.6 keV.

in scattering, which in turn, causes an extra broadening effect (~ 4 meV for peak 1).

The data shown in Table II indicate that following exposure to a 10 MRad ^{60}Co gamma source, there was an observed increase in the value of φ_{LO} , while the values of φ_{imp} exhibited a reduction. The changes in the E_{ph} (LO phonon energy) values for the reference and irradiated samples are within the error margin of the fit results. The values of E_i and Γ_0 showed minimal variations across all peaks, suggesting that exposure to a ^{60}Co gamma source did not result in the introduction of any extra defects or impurities. Moreover, it did not enhance the inhomogeneity in the crystal's size, shape, or composition. Additionally, the obtained fits resulted in significantly low values of φ_A ($0.116 - 0.215 \mu\text{eV/K}$), corresponding to $\sim 0.035 - 0.064$ meV at 300 K, implying that the impact of acoustic phonons on the broadening of the spectrum was negligible. Given the comparatively weaker exciton-acoustic phonon coupling, it is evident that the exciton-longitudinal optical (LO) phonon interaction, combined with the presence of native defects and impurities, contributes mostly to homogeneous linewidth broadening [the last two terms of Eq. (3)].

Table II additionally reveals that the LO phonon energies are larger than the thermal energy at 300 K (≈ 25 meV). Consequently, under elevated temperatures, a single LO phonon can be absorbed by the lowest lying exciton via a Fröhlich interaction with energy E_{ph} . It then has the potential to dissociate into free charge carriers or scatter with other particles in the same bound state or with distinct excitonic states.²¹ Each of these processes is governed by the corresponding exciton binding energy.

The aforementioned results suggest that the structural integrity of CsPbBr_3 is largely unaltered following exposure to a 10 MRad dose of ^{60}Co irradiation. An analogous observation was made for a prior sample that had been subjected to a dose of 100 kRad from a ^{60}Co irradiation source. Moreover, crystals from the VK59A ingot have exhibited appreciable spectral sensitivity and good detector performance.⁹

Study on the defects of perovskite CsPbBr_3 samples through thermally stimulated current (TSC) spectroscopy

Thermally stimulated current (TSC) spectroscopy is used to study electronic traps in the crystal samples. Comparative and in-depth analysis of various CsPbBr_3 crystals demonstrates that the TSC technique is sensitive to defect densities on the order of $10^{11}/\text{cm}^3$ and can differentiate defect levels with a one order of magnitude difference in trap concentrations. Further details of TSC can be found in our recent report.²²

Trace amounts of defects, in the parts per billion range, can significantly affect charge transport and recombination lifetime. Thermally stimulated current (TSC) spectroscopy is one of the characterization techniques with the sensitivity required for defect detection in semiconductors.²³ TSC spectroscopy has proven to be useful in the analysis of semi-insulating semiconductors. TSC has been employed in CdZnTe defect studies.²⁴

In this study, we conducted thermally stimulated current (TSC) measurements within a temperature range of 80–320 K. The objective was to identify and compare deep level defects in bulk

halide perovskite single crystals of CsPbBr_3 , which were synthesized using the Bridgman growth technique. Spectral information from TSC was analyzed using the simultaneous multipeak analysis (SIMPA) method.^{25,26}

Trap energy and concentration can be estimated by examining the current peak's temperature and intensity. The utilization of the simultaneous multiple peak analysis (SIMPA) approach was employed to extract information on the energy level of the trap (E_{Ti}), capture cross section (σ_i), and trap density (N_{Ti}) within the TSC spectrum.

The approximate trap energy is determined by the temperature corresponding to the peak's maximum. Using a quasi-equilibrium approach,²⁷ the energy level of an electron trap E_{Ti} is given by²⁸

$$E_{Ti} = kT_m \ln \left(\frac{T_m^4}{\beta} \right). \quad (4)$$

The collected charge for trap i (Q_{Ti}), which is given by

$$Q_{Ti} = \int I_{TSC}^i dt, \quad (5)$$

which can be used to approximate the trap concentration N_{Ti} . Here, I_{TSC}^i is the collected current for trap i and Q_{Ti} is the temporal integration of each TSC peak. The concentration N_{Ti} is given by

$$N_{Ti} = \frac{Q_{Ti}}{2\mu\tau eAE}, \quad (6)$$

where $\mu\tau$ is the carrier mobility-lifetime product, e is the electron charge, A is the electrode area, and E is the applied electric field. Using (4) and (5), the trap depths were calculated.

TSC is measured by a Keithley current meter when temperature increases in a controlled manner from ~ 80 to 300 K after the sample is exposed to the Xe arc lamp at ~ 80 K temperature. Figure 7 shows the datasets of TSC signal vs temperature of a reference CsPbBr_3 sample VK74a-12, as compared to that of a CsPbBr_3 sample IP21009-5-7, irradiated under an x-ray beam at the Advanced Photon Source (APS) source at Argonne National Laboratory.

Table III shows the fit results of the TSC measurement for the reference CsPbBr_3 sample VK74a-12 up to room temperature ~ 300 K. The total number of traps in the 79–300 K temperature range is $\sim 0.46 \times 10^{13}$ per cm^3 . For comparison, the TSC datasets of the CsPbBr_3 sample IP21009-5-7, irradiated by 58.6 keV x-ray of

TABLE III. Results of the TSC measurement for the reference CsPbBr_3 sample VK74a-12.

T_m (K)	ΔE_i (eV)	$N_T (\times 10^{11} \text{ cm}^{-3})$	Potential defects
89.1–99.1	0.160–0.180	7.49	V_{Cs}
122.3	0.233	3.35	Pb_i
154.2–179.8	0.306–0.366	1.16	Impurities
217.9–241.8	0.458–0.517	23.60	Pb_{Br}
256.7–271.7	0.554–0.592	8.12	Impurities
291.9–302.8	0.643–0.671	1.97	Impurities

30 December 2023 08:30:28

TABLE IV. TSC measurement for the CsPbBr₃ sample IP21009-5-7, irradiated under a 58.6 keV x-ray beam.

T_m (K)	ΔE_i (eV)	N_T ($\times 10^{11}/\text{cm}^3$)	Potential defects
83.55–90.19	0.148–0.162	3.52	V_{Cs}
108.56–142.15	0.202–0.278	2.51	Pb_i
150.94–214.6	0.298–0.450	4.87	Impurities
230.10	0.488	12.50	Pb_{Br}
251.30–277.80	0.540–0.607	6.68	Impurities
286.30	0.629	1.17	Pb_{Br}
297.80–310.60	0.658–0.691	2.79	Impurities

flux $2.2 \times 10^{12} \text{ p s}^{-1} \text{ mm}^{-2}$, were fitted as well. Table IV shows the fit results of the TSC measurement for this sample up to room temperature ~ 300 K. The total number of traps in the temperature range of 79–300 K is $\sim 0.34 \times 10^{13}$ per cm^3 .

In both samples, deep trap levels were detected within the energy range of 0.16–0.67 eV. Nonetheless, in the energy range, both the irradiated CsPbBr₃ detector crystal and the reference non-irradiated CsPbBr₃ detector crystal reveal similar defect concentrations. Comparable defect density magnitude across the TSC measurement range of 79–315 K suggests that intense flux irradiation did not generate substantial defects. Consequently, the CsPbBr₃ detector crystals are robust.

The presence of native defects resulting from non-stoichiometry can have a notable impact.²⁹ Possible traps in these halide perovskites include lead interstitials Pb_i with energies between 0.21 and 0.27 eV and bromine on lead (Pb_{Br}) antisite defects with energies between 0.48 and 0.62 eV. Cesium vacancies (V_{Cs}) also have a low formation energy and defect energy of 0.17 eV. The high vapor pressure of Br in melt growth conditions allows for the formation of V_{Br} vacancies. The present study, however, did not yield evidence supporting the existence of Br vacancies. The V_{Br} defect is characterized by its shallow nature and resonance with the energy bands. However, its observation necessitates lower temperatures (below 79 K), which is beyond the operational limitations of our existing TSC setup. In general, deep level defects in the material can behave as charge carrier traps, decreasing mobility and causing charge carriers to recombine with each other before collection.³⁰ In comparison to the previous measurements conducted by Zhang *et al.*⁷ on bulk CsPbBr₃, our samples exhibit lower trap concentrations.

The observed low densities of deep level defects in these crystals align with the finding that both ingots (VK74a and IP21009) have exhibited appreciable radiation detector performance upon exposure to high-energy radiation.¹⁰ By employing the trap parameters obtained from TSC spectroscopy as a means of feedback for the process of crystal growth, it is possible to reduce the presence of undesirable defect states. This, in turn, leads to crystal samples that exhibit enhanced mobilities, longer carrier lifetimes, and improved spectral response characteristics.

CONCLUSIONS

In this study, we investigated the defect properties of CsPbBr₃ perovskite compound samples using low temperature and room

temperature photoluminescence and thermally stimulated current spectroscopies. At ambient temperature, PL spectroscopy demonstrates an enhanced sensitivity to detect defects that are situated in close proximity to each other on the surface of a specific sample. The PL data reveal a discernible correlation between excitation intensities, suggesting that the observed emission stems from the radiative recombination of excitons. Bridgman-grown CsPbBr₃ halide perovskite single crystals were also analyzed using low temperature PL. A band tail or Urbach-like tail was observed in the spectrum of the PL signal below the band edge. The temperature and excitation dependencies of the emission bands suggest that they arise from the radiative recombination of both free excitons and trapped/bound excitons. As with other perovskites, the analysis of temperature-dependent PL data provides evidence that LO phonon scattering via the Fröhlich interaction is mainly responsible for the thermal broadening of exciton linewidth in these halide perovskite crystals, with an additional contribution in our crystals due to the presence of ionized impurities. The existence of these edge states may be attributed to point defects such as metal/halide vacancies and interstitials, as well as twinning, resulting from the cubic-to-tetragonal phase transition in CsPbBr₃.

Thermally stimulated current (TSC) spectroscopy effectively assessed CsPbBr₃ crystal defect levels and concentrations. The origins and trap characteristics of CsPbBr₃ crystals were tentatively attributed to both intrinsic point defects and impurities. Crystals of CsPbBr₃, possessing a total trap concentration of approximately $1.0 \times 10^{13} \text{ cm}^{-3}$, have exhibited appreciable sensitivity to high-energy gamma radiation. The utilization of trap parameters obtained from PL and TSC spectroscopy, as a means of feedback for crystal formation, enables the detection of undesirable defect states. Consequently, this produces crystal samples with extended carrier lifetimes and improved spectral response characteristics.

SUPPLEMENTARY MATERIAL

See the supplementary material for (1) the crystal growth procedure using the melt process, TSC sample fabrication; (2) photoluminescence measurements; (3) the evaluation of mobility lifetime products; (4) the procedure for conducting TSC measurements; and (5) the irradiation of samples with radiation sources.

ACKNOWLEDGMENTS

The authors thank Nathan Liu for technical assistance. This research was sponsored by the Defense Threat Reduction Agency (DTRA) as part of the Interaction of Ionizing Radiation with Matter University Research Alliance (IIRM-URA) under Contract No. HDTRA1-20-2-0002. ⁶⁰Co gamma irradiation was performed at the Pennsylvania State University Radiation Science and Engineering Center (RSEC). The study utilized the resources of the Advanced Photon Source (a U.S. DOE Office of Science user facility operated for the DOE Office of Science by Argonne National Laboratory) under Contract No. DE-AC02-06CH11357. This work made use of the NUFAB-Cook facility of Northwestern University's NUANCE Center, which has received support from the SHyNE Resource (NSF ECCS-2025633), the IIN, and Northwestern's MRSEC program (NSF DMR-2308691).

AUTHOR DECLARATIONS

Conflict of Interest

The authors have no conflicts to disclose.

Author Contributions

Zhifu Liu: Data curation (equal); Formal analysis (equal); Investigation (equal); Methodology (equal); Validation (equal); Writing – original draft (equal); Writing – review & editing (equal). **John A. Peters:** Data curation (equal); Formal analysis (equal); Investigation (equal); Methodology (equal); Validation (equal); Writing – original draft (equal); Writing – review & editing (equal). **Khasim Saheb Bayikadi:** Resources (equal). **Vladislav Klepov:** Resources (equal). **Lei Pan:** Resources (equal). **Indra Raj Pandey:** Resources (equal). **Mercouri G. Kanatzidis:** Funding acquisition (equal); Project administration (equal); Supervision (equal). **Bruce W. Wessels:** Conceptualization (equal); Funding acquisition (equal); Project administration (equal); Supervision (equal); Writing – review & editing (equal).

DATA AVAILABILITY

The data that support the findings of this study are available from the corresponding authors upon reasonable request.

REFERENCES

- ¹Y. He, M. Petryk, Z. Liu, D. G. Chica, I. Hadar, C. Leak, W. Ke *et al.*, “CsPbBr₃ perovskite detectors with 1.4% energy resolution for high-energy γ -rays,” *Nat. Photonics* **15**(1), 36–42 (2021).
- ²Y. He, L. Matei, H. J. Jung, K. M. McCall, M. Chen, C. C. Stoumpos, Z. Liu *et al.*, “High spectral resolution of gamma-rays at room temperature by perovskite CsPbBr₃ single crystals,” *Nat. Commun.* **9**(1), 1609 (2018).
- ³C. C. Stoumpos, C. D. Malliakas, J. A. Peters, Z. Liu, M. Sebastian, J. Im, T. C. Chasapis *et al.*, “Crystal growth of the perovskite semiconductor CsPbBr₃: A new material for high-energy radiation detection,” *Cryst. Growth Des.* **13**(7), 2722–2727 (2013).
- ⁴M. Bruzzi, F. Gabelloni, N. Calisi, S. Caporali, and A. Vinattieri, “Defective states in micro-crystalline CsPbBr₃ and their role on photoconductivity,” *Nanomaterials* **9**(2), 177 (2019).
- ⁵A. Owens and A. Peacock, “Compound semiconductor radiation detectors,” *Nucl. Instrum. Methods Phys. Res. B* **531**(1–2), 18–37 (2004).
- ⁶L. Alwafi, A. Datta, J. M. Pientka, and B. Barman, “Excitation wavelength dependent photon emission and phase change probing in CsPbBr₃ quantum dots,” *Solid State Commun.* **366–367**, 115136 (2023).
- ⁷M. Zhang, Z. Zheng, Q. Fu, P. Guo, S. Zhang, C. Chen *et al.*, “Determination of defect levels in melt grown, all inorganic perovskite CsPbBr₃ crystals by thermally stimulated current spectra,” *J. Phys. Chem. C* **122**(19), 10309–10315 (2018).
- ⁸K. S. Bayikadi *et al.*, “Advancing gamma-ray detection: Understanding stability and efficiency of CsPbBr₃ perovskite semiconductor,” in *2023 IIRM-URA Annual Technical Review*, University Park, Pennsylvania (Pennsylvania State University, 2003).
- ⁹M. C. De Siena, V. V. Klepov, S. P. Stepanoff, K. S. Bayikadi, L. Pan, I. R. Pandey, S. Karki, D. Y. Chung, D. E. Wolfe, and M. G. Kanatzidis, “Extreme γ -ray radiation tolerance of spectrometer-grade CsPbBr₃ perovskite detectors,” *Adv. Mater.* **35**(38), 2303244 (2023).
- ¹⁰L. Pan, Z. Liu, C. Welton, V. V. Klepov, J. A. Peters, M. C. De Siena, A. Benadia, I. Pandey, A. Miceli, D. Y. Chung, G. M. Reddy, B. W. Wessels, and M. G. Kanatzidis, “Ultrahigh-flux x-ray detection by a solution-grown perovskite CsPbBr₃ single-crystal semiconductor detector,” *Adv. Mater.* **35**(25), 2211840 (2023).
- ¹¹J. A. Peters, Z. Liu, O. Bulgin, Y. He, V. Klepov, M. De Siena, M. G. Kanatzidis, and B. W. Wessels, “Excitons in CsPbBr₃ halide perovskites,” in *Metal-Halide Perovskite Semiconductors*, edited by Nie W. and K. Iniewski (Springer Nature Publisher, 2023), Chap. 5. ISBN: 978-3-031-26891-5.
- ¹²D. Bimberg, M. Sondergeld, and E. Grobe, “Thermal dissociation of excitons bounds to neutral acceptors in high-purity GaAs,” *Phys. Rev. B* **4**(10), 3451 (1971).
- ¹³W. Gao, X. Gao, T. A. Abtew, Y.-Y. Sun, S. Zhang, and P. Zhang, “Quasiparticle band gap of organic-inorganic hybrid perovskites: Crystal structure, spin-orbit coupling, and self-energy effects,” *Phys. Rev. B* **93**(8), 085202 (2016).
- ¹⁴M. Baranowski, J. M. Urban, N. Zhang, A. Surrente, D. K. Maude, Z. Andaji-Garmaroudi, S. D. Stranks, and P. Plochocka, “Static and dynamic disorder in triple-cation hybrid perovskites,” *J. Phys. Chem. C* **122**(30), 17473–17480 (2018).
- ¹⁵K. Wei, Z. Xu, R. Chen, X. Zheng, X. Cheng, and T. Jiang, “Temperature-dependent excitonic photoluminescence excited by two-photon absorption in perovskite CsPbBr₃ quantum dots,” *Opt. Lett.* **41**(16), 3821–3824 (2016).
- ¹⁶A. Musienko, J. Čížek, H. Elhadidy, P. Praus, K. Higgins, B. Dryzhakov, A. Kanak *et al.*, “Origin of defects and positron annihilation in hybrid and all-inorganic perovskites,” *Chem. Mater.* **34**(1), 297–306 (2022).
- ¹⁷O. Yaffe, Y. Guo, L. Z. Tan, D. A. Egger, T. Hull, C. C. Stoumpos, F. Zheng *et al.*, “Local polar fluctuations in lead halide perovskite crystals,” *Phys. Rev. Lett.* **118**(13), 136001 (2017).
- ¹⁸D. Han, K. Yang, C. Bai, F. Chen, Z. Sun, Y. Wang, H. Ji, Z. Yang, and X. Tang, “Thermal and chemical durability of metal halide perovskite CsPbBr₃ single crystals,” *Chem. Eng. J.* **475**, 146209 (2023).
- ¹⁹M. Liao, B. Shan, and M. Li, “*In situ* Raman spectroscopic studies of thermal stability of all-inorganic cesium lead halide (CsPbX₃, X = Cl, Br, I) perovskite nanocrystals,” *J. Phys. Chem. Lett.* **10**(6), 1217–1225 (2019).
- ²⁰R. Saran, A. Heuer-Jungemann, A. G. Kanaras, and R. J. Curry, “Giant bandgap renormalization and exciton-phonon scattering in perovskite nanocrystals,” *Adv. Opt. Mater.* **5**, 1700231 (2017).
- ²¹H. D. Sun, T. Makino, N. T. Tuan, Y. Segawa, M. Kawasaki, A. Ohtomo, K. Tamura, and H. Koinuma, “Temperature dependence of excitonic absorption spectra in ZnO/Zn_{0.88}Mg_{0.12}O multiquantum wells grown on lattice-matched substrates,” *Appl. Phys. Lett.* **78**(17), 2464–2466 (2001).
- ²²Z. Liu, J. A. Peters, L. Pan, V. Klepov, M. De Siena, A. Benadia, D. Y. Chung, M. G. Kanatzidis, and B. W. Wessels, “Investigation of defects in melt and solution grown perovskite CsPbBr₃ single crystals,” *Appl. Phys. Lett.* **122**(13), 131902 (2023).
- ²³M. Pavlović and U. V. Desnica, “Precise determination of deep trap signatures and their relative and absolute concentrations in semi-insulating GaAs,” *J. Appl. Phys.* **84**(4), 2018–2024 (1998).
- ²⁴M. Pavlović, M. Jakšić, H. Zorc, and Z. Medunić, “Identification of deep trap levels from thermally stimulated current spectra of semi-insulating CdZnTe detector material,” *J. Appl. Phys.* **104**(2), 023525 (2008).
- ²⁵D. C. Look, “The electrical and photoelectronic properties of semi-insulating GaAs,” in *Semiconductors and Semimetals* (Elsevier, 1983), Vol. 19, pp. 75–170.
- ²⁶U. V. Desnica, M. Pavlović, Z.-Q. Fang, and D. C. Look, “Thermoelectric effect spectroscopy of deep levels in semi-insulating GaN,” *J. Appl. Phys.* **92**(7), 4126–4128 (2002).
- ²⁷R. H. Bube, *Photoconductivity in Solids* (Wiley, New York, NY, 1960).
- ²⁸Z. Fang, L. Shan, T. E. Schlesinger, and A. G. Milnes, “Study of defects in LEC-grown undoped Si-GaAs by thermally stimulated current spectroscopy,” *Mater. Sci. Eng. B* **5**(3), 397–408 (1990).
- ²⁹J. Kang and L.-W. Wang, “High defect tolerance in lead halide perovskite CsPbBr₃,” *J. Phys. Chem. Lett.* **8**(2), 489–493 (2017).
- ³⁰G. F. Knoll, *Radiation Detection and Measurement* (John Wiley & Sons, 2010).